

FEATURE ARTICLE

Cage Exit versus Cage-Induced Reaction upon Photodissociation of Matrix-Isolated H₂S:
Experiment and Statistical Theory

J. Zoval and V. A. Apkarian*

*Department of Chemistry, University of California, Irvine, California 92717**Received: April 4, 1994; In Final Form: June 13, 1994**

In its first absorption continuum, a variety of channels are available to the permanent dissociation of matrix-isolated H₂S, the two main ones being cage exit to yield SH + H and the cage-induced bimolecular reaction SH + H → S + H₂. Laser-induced fluorescence (LIF) from SH(A→X) and S(¹S→¹D) is used to probe each of these channels. LIF of S atoms is a site-specific probe that can distinguish among interstitial and substitutional sites and sites at which the S and H₂ products are crowded together. In addition to substitutionally trapped S atoms, interstitial trapping is observed. The latter implies cage exit of S(¹D). In the crowded sites, the LIF signal from S is stable, implying that there is an activation barrier to reaction of S(¹D) with H₂. In Kr, the SH:S branching ratio increases monotonically from 0.7 to 3 for excess energies between 1 and 2.5 eV. The quantum yield of the S channel is nearly independent of photodissociation energy, while the SH channel yield increases monotonically with excess energy. A statistical model, based on cones of reactivity, is used to rationalize the branching of the cage-induced reaction H + SH to yield H₂S or S + H₂. A statistical theory for sudden cage exit, which incorporates barrier height distributions due to zero-point and thermal fluctuations of the lattice, is presented and used to characterize the nature of cage exit dynamics. At large excess energies sudden exit becomes the dominant channel. However, it is clear that near threshold the fragment exits over a deformed barrier, after extensive energy transfer to the lattice. The treatment is successful in predicting known energy, temperature, isotope, and mass asymmetry effects controlling sudden photodissociation dynamics of hydrides.

I. Introduction

As prototypes of condensed-phase reactive dynamics, the photodissociation of hydrides in van der Waals solids has been the focus of both experimentation and theory. The description of permanent bond breaking in these systems is, for the most part, controlled by the cage exit dynamics of the H atom. Given the existence of reliable H–Rg potentials, and its isotropic nature, the system is amenable to simulations, and one could hope for rigorous models to emerge by iteration between experiment and theory. Despite these considerations, the description of the mechanism of H atom cage exit seems to be the subject of controversy.

First by classical molecular dynamics simulations, and subsequently by mixed quantum/classical simulations,² the photodissociation of HI in solid Xe was originally introduced as a prototype. Typical trajectories in the simulations showed that the H atom exit is “delayed” and occurs over a reduced barrier caused by the opening of a passage after the cage atoms are set in motion by the cumulative energy loss of photofragments.¹ Due to complications arising from ionic channels,^{3,4} this system has proved to be a poor choice for experimental scrutiny, and although a significant amount of work has been carried out in both crystalline solids and matrices,^{5,6} little has been learned about the details of dissociation via covalent repulsive surfaces. Experimental rigor was first provided by a series of systematic studies on the photodissociation of H₂O/D₂O in Ar, Kr, and Xe matrices, as a function of excess energy and temperature.^{7–11} The energy dependence of quantum yields was indicative of “sudden” cage exit of H, in apparent contradiction with the delayed exit scenario suggested by the HI/Xe simulations. This thesis was supported by presenting a qualitative prediction for sudden exit

dynamics near the threshold of a sharp barrier to dissociation—a quadratic power law for quantum yields with an isotope dependence H/D ~ 2—which was in acceptable agreement with experiments.⁷ However, the observed temperature dependence of quantum yields was interpreted by a local heating model,¹⁰ in contradiction with the sudden thesis, since exit after energy transfer to the cage is necessarily implied. In a more recent molecular dynamics simulation of HCl dissociation in Xe, which for the first time included recombination and nonadiabatic effects, contributions from both sudden and delayed exit were noted to contribute to the cage exit yield.¹² These simulations also showed that cage exit could occur for H fragments initially generated at excess energies below the cage barrier, reinforcing the notion of delayed exit after deformation of the cage.¹² In more recent experimental studies on matrix-isolated H₂S, we noted that photodissociation thresholds were limited by the absorption threshold, and cage exit occurred at excess energies far below what may be expected as the potential barrier of the undistorted cage.¹³ This implied exit over a barrier which is not strictly potential in nature and therefore incompatible with the sudden model.

The expectation that there be a universal description of photodissociation of hydrides in rare gas solids may be somewhat misguided. Understanding the differences in observed behavior and extracting the information contained in experiment and simulation remain a challenge. Clear definitions of terminology, as in “sudden” versus “delayed” exit, are necessary, and statistical treatments that describe such limiting behaviors are quite crucial for further discourse. Comparisons with such models may allow the assessment of the significance of observations, whether through experiment or simulation. In this context, it is important to point out that simulations suffer from a significant shortcoming. At the cryogenic temperatures of interest, zero-point energy can be

* Abstract published in *Advance ACS Abstracts*, July 15, 1994.

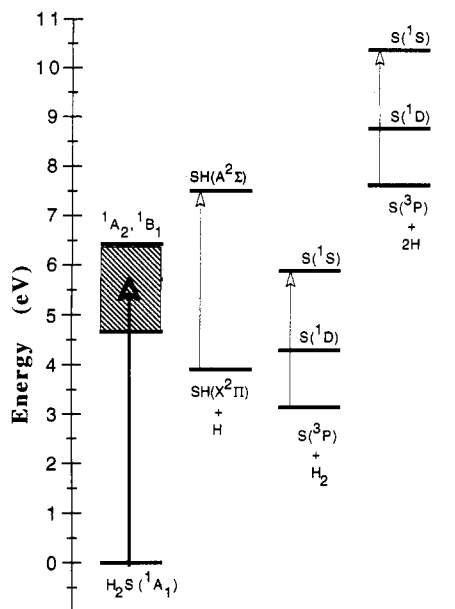


Figure 1. Energy level diagram of possible products formed upon photodissociation of H_2S . The shaded area represents the range of photodissociation energies.

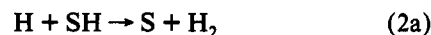
expected to play a significant role in dynamics; yet at present, there are no tested methods that incorporate this quantum effect correctly in many-body simulations. Quantum statistics can of course be included in statistical treatments, and as we will show is rather crucial to the problem at hand. The development of a clear picture for the photodissociation of hydrides in crystalline rare gases is the chief aim of this paper. We pursue this aim relying on more recent data on photodissociation of H_2S isolated in Ar and Kr matrices, which in addition to cage exit dynamics allows the scrutiny of in-cage dynamics of the recoiling photo-fragments.

With diatomics in mind, photodissociation studies in van der Waals solids and clusters have for the most part concentrated on cage exit dynamics of fragments.¹⁴ Already in the case of triatomics, neither cage exit is essential for permanent dissociation, e.g., in-cage dissociation of N_2O to yield $\text{N}_2(\text{X}) + \text{O}(^3\text{P})$;¹⁵ nor does caging of fragments lead strictly to recombination. Isomerization will occur where possible. The classic case of OCIO isomerization to yield ClOO is an example,¹⁶ among many known in the literature on matrix isolation spectroscopy.¹⁷ The photodissociation of H_2S in rare gas solids allows the study of both cage exit dynamics of H atoms and cage-induced bimolecular reactions in highly constrained environments. The latter is obviously an outcome of the lingering of energetic fragments within the parent cage. In our earlier report we already noted that, upon excitation to its first absorption continuum, permanent dissociation of H_2S in rare gas solids proceeds via two distinct channels:¹³



The overall quantum yield of dissociation of H_2S was reported there as a function of excitation energy. The branching ratio between these two product channels in Kr has been determined since then and will be reported here. Determination of absolute probabilities of these individual channels is necessary to separate the cage exit process from overall dissociation. In the wavelength range of the present studies, 250–193 nm, the photodissociation of H_2S in the gas phase proceeds promptly to yield $\text{SH}(\text{X}) + \text{H}$. The molecular potential energy surfaces of H_2S in this energy range have been extensively studied. Although the $\text{S} + \text{H}_2$ channel is energetically accessible (see Figure 1), the theoretical potential energy surfaces show insufficient torque acting on fragments to

lead to $\text{S} + \text{H}_2$ formation in the free molecule.¹⁸ Thus, this observed channel is a condensed-phase effect, the result of the constrained environment in which the photoexcitation is carried out. After the initial impulsive impact of the H photofragment with the lattice, recoil and in-cage energy loss on the various electronic surfaces that correlate with $\text{SH}(\text{X}) + \text{H}$ are necessary for the formation of the $\text{S} + \text{H}_2$ product. In essence, it is possible to regard SH as an efficient scavenger of H in the cage-induced bimolecular reaction



in which geminate fragments are induced either to react (2a) or to recombine (2b) by the cage. We also determine the branching ratio between these cage-induced bimolecular reactions and show that they are mainly governed by steric factors, namely, by the probability that the activated caged pair lose its energy while the fragments are in different reaction cones. The concept of reaction cones, which has been extensively used in gas-phase reactive dynamics, is also useful in the treatment of condensed-phase bimolecular reactions, as already pointed out in the literature.¹⁹

In time-independent studies of reactive dynamics in solids, characterization of reagent trapping sites, product trapping sites, and probabilities of individual channels are the sought quantities. We rely on infrared spectroscopy to establish isolation and characterization of the local dynamics of the parent molecule.¹³ Laser-induced fluorescence (LIF) is used as a site-specific probe for both determination of probabilities of individual reactive channels and to establish product sites. The experimental method can be understood by referring to the energy level diagram in Figure 1. Photodissociation of H_2S isolated in Kr matrices is carried out by tunable ultraviolet lasers. The production of SH and S is monitored by LIF. The SH fragment is followed by excitation of the $\text{SH}(\text{A} \leftarrow \text{X})$ transition, while monitoring the Stokes-shifted $\text{SH}(\text{A} \rightarrow \text{X})$ emission. In contrast with the gas phase, the electronic predissociation of $\text{SH}(\text{A})$ is completely blocked in Kr; hence, this transition can be used as a sensitive probe of the fragment yield. Details of the spectroscopy and caging of electronic predissociation of SH trapped in Ar and Kr have already been reported.²⁰ The S fragment is followed by excitation of the atomic $^1\text{S} \leftarrow ^3\text{P}$ transition while monitoring the $^1\text{S} \rightarrow ^1\text{D}$ emission. These transitions, while strongly forbidden in the isolated atom, are enhanced by the matrix and therefore enable a convenient detection scheme for atomic sulfur. Given the extent of perturbation, the probed transitions should be regarded as belonging to Kr_nS , in close analogy with the energetics of O atoms trapped in heavy rare gases, which was recently treated in some detail.²¹ Note, in the energy range of the studies, the $\text{S} + \text{H} + \text{H}$ product is inaccessible from H_2S (see Figure 1). However, once SH is formed, it is possible to dissociate it in Kr by a two-photon process.¹³ Using this two-step process, photodissociation of H_2S followed by two-photon dissociation of SH, it is possible to completely convert H_2S to S. This is the key to the method used here for obtaining branching ratios. It has not been possible to implement the same measurements in Ar for reasons that are not fully understood. As such, in Ar, only overall dissociation quantum yields are available at present.

II. Experimental Section

The experimental details are nearly identical to those described in ref 13. Pulsed deposition is used to prepare H_2S -doped Kr matrices on a rhodium-coated copper substrate. Isolation of H_2S is verified by both IR spectroscopy and verifying the absence of S_2 formation upon irradiation of the samples.¹³ A variety of lasers are used to dissociate H_2S and to probe the S and SH products. The branching ratios are obtained by the following sequence of measurements: (a) H_2S is dissociated, and the SH or S product growth is followed by its LIF signal. For this purpose,

the dissociation laser (250–193 nm) and the product probe (332 nm for SH and 450 nm for S) are overlapped on the solid. (b) After completing the H₂S dissociation, the S atom excitation spectrum is collected while monitoring its total fluorescence. (c) SH is then dissociated by high-intensity irradiation ($\sim 2 \text{ mJ cm}^{-2} \text{ pulse}^{-1}$) at 332 nm. This process is also followed by either monitoring the decay of SH fluorescence or monitoring the growth of LIF from S. (d) After SH is converted to S by photodissociation, the excitation spectrum of S is recorded again.

The two S atom excitation spectra obtained in (b) and (d) measure the S atom produced in the photodissociation of H₂S versus the total S atom signal for complete conversion of H₂S to S. These are sufficient to establish absolute quantum yields of the individual permanent dissociation channels.

III. Results

Upon photodissociation of H₂S in Kr, emission from S(¹S \rightarrow ¹D) can be observed when the sample is excited near the atomic S(¹S \leftarrow ³P) transition, which occurs at 451 nm in vacuum.²² A typical emission spectrum is shown in Figure 2a. This emission has previously been assigned by Taylor and Walker to matrix-perturbed S(¹S \rightarrow ¹D).²³ Excitation spectra obtained by monitoring this emission (Figure 2b) show a broad resonance and evidence for two sites in the matrix, one peaking near 461 nm and another near 456 nm. These are identified as I and II in Figure 2b. Indeed both emission lifetimes and line shapes are different for these two different sites. Figure 2a shows the emissions associated with each of the sites. At 16 K, site II has a lifetime of 12 μs while site I has a lifetime of 64 μs . The fluorescence lifetime of site I shows a mild temperature dependence, varying from 64 μs at 16 K to 47 μs at 41 K. Upon warm-up to 20 K, the high-energy site is quantitatively converted to the lower energy site as illustrated in Figure 2b. The relative populations of these two different sites depend on matrix history and are subject to significant variation from sample to sample and from spot to spot within the same matrix. A general trend of reduction in the population of the high-energy site with increased photon energy is seen but could not be reproduced quantitatively in different experiments. When the matrix is further annealed at successively higher temperatures for short periods of time (above 25 K, S atoms diffuse and form S₂), the excitation spectrum shown in Figure 2c is obtained. The spectrum shows a well-defined zero-phonon line at 21 663 cm⁻¹ and a structured phonon sideband. Emission spectra and fluorescence lifetimes obtained by excitation throughout this line profile are identical.

The S atom spectroscopy in solid Ar parallels that of Kr. An excitation spectrum from a partially annealed sample is shown in Figure 2d. As in Kr, prior to annealing, two sites are clearly observed as illustrated in the inset to Figure 2d. The zero-phonon line in the stable site now appears at 457.27 nm, shifted from the Kr position by $\sim 200 \text{ cm}^{-1}$, and prominent phonon sidebands are observed with differ from that of Kr in their detail. From limited temperature dependence studies, which show the appearance of absorptions to the red of the zero phonon line, we infer the presence of thermal population of the matrix split m_J states of the S(³P₂) electronic ground manifold. Since the ¹S state has spherical symmetry, and its interaction with rare gas atoms is expected to be rather weak, we expect the excited state to show a potential minimum at cage center. The observation of phonon activity in the excitation ¹S \leftarrow ³P spectrum is then indicative of eccentric potential minima in the ground state. The details of these spin-orbit split surfaces we believe hold the key to understanding the structured phonon sidebands and also the unusually high mobility of chalcogens in rare gas solids.²⁴

The photodissociation of H₂S was followed by monitoring the growth of LIF from both SH and S as a function of irradiation time. This is shown in the first part of the growth curve in Figure 3. After H₂S dissociation the same volume is irradiated with 332-nm pulses at an intensity of $1.2 \times 10^{16} \text{ photons cm}^{-2} \text{ pulse}^{-1}$

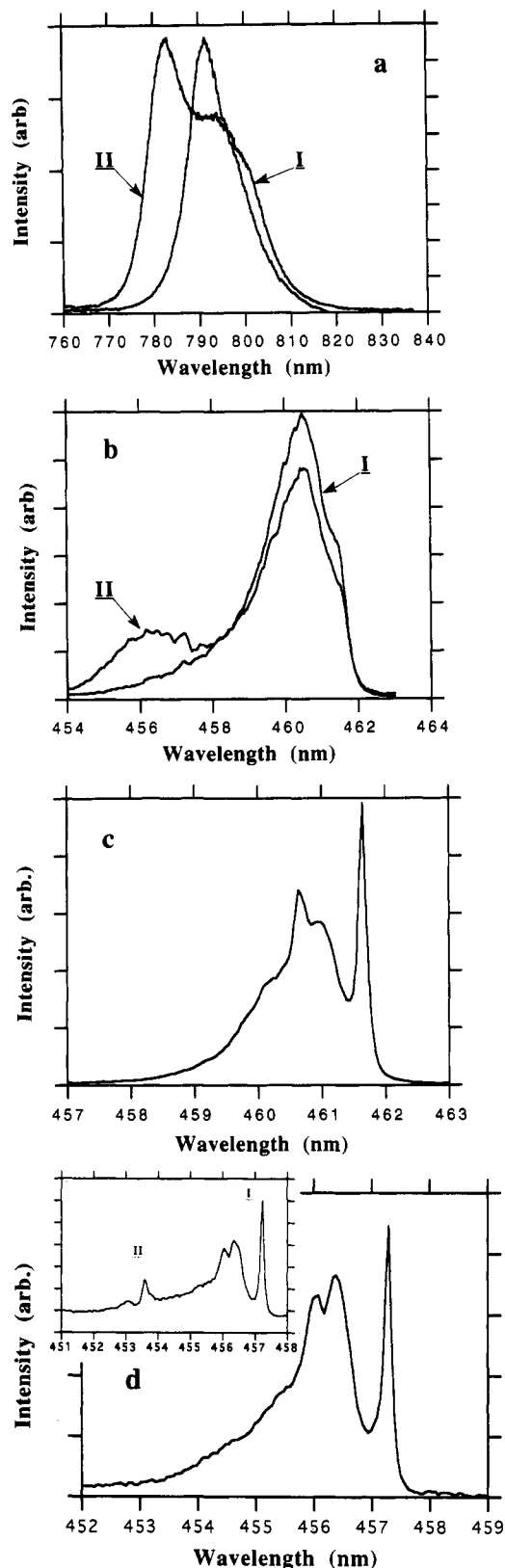


Figure 2. Emission and excitation spectra of S Atom in a krypton matrix generated by photodissociation of H₂S (M/R = 10 000). (a) Emission spectra generated upon excited of stable (460 nm) and unstable (456 nm) sites at 15 K. (b) S(¹S \leftarrow ³P) excitation spectra in krypton, obtained by monitoring the ¹S \rightarrow ¹D emission at 792 nm with a band-pass of 13 nm. The spectrum which shows both sites was recorded at 15 K, immediately after dissociation of H₂S. Upon warming up to 20 K and recooling to 15 K, site II interconverts to site I. The integrated area of the excitation band is preserved, while the site II band at 456 nm disappears. (c) A fully annealed S(¹S \leftarrow ³P) excitation spectrum in krypton. Same as in (b) however after annealing by a temperature cycle of 15 K–35 K–15 K. (d) Excitation spectrum of the stable site S(¹S \leftarrow ³P) in solid Ar, recorded at 16 K after annealing at 20 K. In the inset an unannealed spectrum is shown, in which the two sites are clearly visible.

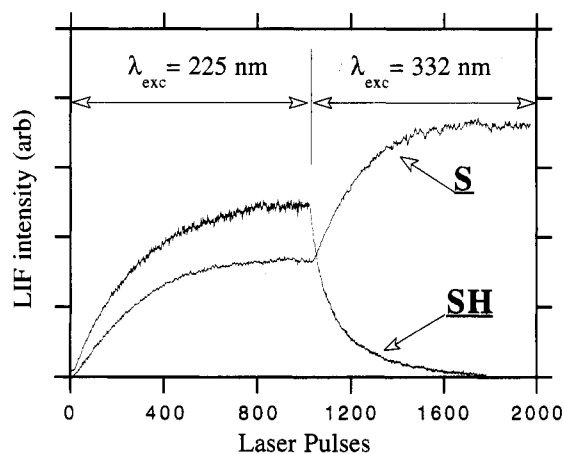


Figure 3. Time evolution of LIF from SH and S as a function of irradiation. S atom and SH LIF signals during the first 1000 pulses are recorded while irradiating the $\text{H}_2\text{S}/\text{Kr}$ at 225 nm (flux = 7.42×10^{14} photons cm^{-2} pulse $^{-1}$). After completion of H_2S dissociation, during the second 1000 pulses, SH is dissociated by excitation at 332 nm (flux $\sim 1.2 \times 10^{16}$ photons cm^{-2} pulse $^{-1}$), and LIF is simultaneously recorded from SH- ($\text{A} \rightarrow \text{X}$) at 417.9 nm and S ($^1\text{S} \rightarrow ^1\text{D}$) at 792 nm (induced by 460-nm excitation).

to dissociate the SH. This process is followed by monitoring both the growth of LIF from S and loss of LIF from SH, as illustrated in Figure 3. Since the disappearance rate of H_2S controls the appearance rates of both SH and S, a single characteristic time constant controls the evolutions of relative concentrations:

$$\frac{d}{dt} \left(\frac{[\text{H}_2\text{S}]}{[\text{H}_2\text{S}]_0} \right) = -\frac{d}{dt} \left(\frac{[\text{SH}]}{[\text{SH}]_\infty} \right) = -\frac{d}{dt} \left(\frac{[\text{S}]}{[\text{S}]_\infty} \right) \quad (3)$$

Thus, in the absence of absolute intensities, the time constants extracted from the exponential growth curves of SH and S should be the same. Within experimental error, $\sim 5\%$, this agreement is observed (see Figure 3).

It is easily established that the photodissociation of SH is a two-photon process. Two photons at 332 nm have sufficient energy to reach several dissociative potentials of SH, including $^2\Delta$, $2^2\Pi$, $2^2\Sigma^+$, $4^2\Sigma^+$, and $4^1\Pi$.^{25,26} Nevertheless, we surmise that the SH dissociation proceeds via ionic potentials, based on the observation that this two-photon dissociation channel is absent in Ar. Thus, the measurements of branching ratios could not be carried out in Ar. The mechanism of this two-photon dissociation in Kr is not well understood. In the present we only use the fact that SH can be quantitatively converted to S by intense irradiation at 332 nm.

As pointed above, the S atom excitation spectrum shows a broad distribution and hints at multiple trapping sites. Accordingly, to obtain correct branching ratios, we integrate excitation spectra obtained by monitoring total fluorescence before, A_i , and after, A_f , photodissociation of the SH photoproduct. Quite clearly, A_f is proportional to the total S content of the irradiated volume and therefore to the sum of SH and S channels, while A_i is proportional to the S channel yield during the initial photodissociation of H_2S . Accordingly

$$\gamma(\text{S}) = \frac{A_i}{A_f} = \frac{\phi(\text{S})}{\phi(\text{S}) + \phi(\text{SH})} \quad (4)$$

in which $\phi(\text{S})$ and $\phi(\text{SH})$ are the quantum yields of reactions 1a and 1b. The branching ratio

$$\frac{\phi(\text{SH})}{\phi(\text{S})} = \frac{A_f - A_i}{A_i} \quad (5)$$

is plotted as a function of excess energy in Figure 4. The error bars are the rms variance of four measurements carried out on four different samples at each energy. The source of scatter in

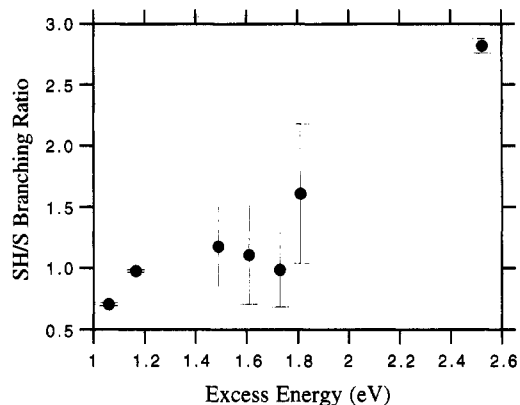


Figure 4. Branching ratio, $\Phi(\text{SH})/\Phi(\text{S})$ in Kr, as a function of excess energy. Each point is the average of four different measurements, carried out in different samples, with and without annealing prior to photodissociation.

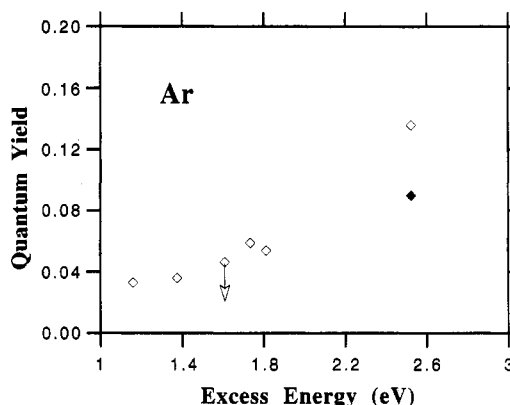


Figure 5. Absolute quantum yields as a function of excess energy, based on total quantum yields from ref 13, and branching ratios of Figure 4. See text for details.

the experimental data is not understood. The method used in the present is sufficiently self-consistent to enable an accuracy of a few percent (error due to relative areas in excitation spectra, before and after SH dissociation). We suspect that charge separation in both S- and SH-doped Kr matrices contributes to systematic errors which not only depend on matrix history but also vary at different irradiation spots in the same solid. Despite the scatter in the data, it is possible to assert that (a) the probabilities of the SH + H and S + H_2 channels are comparable throughout the studied range of photodissociation energies and (b) the SH/H branching ratio is a gently increasing function of excess energy, ranging from 0.7 to 3 for excess energies ranging between 1 and 2.5 eV.

Photodissociation quantum yields were measured in Ar. These are shown in Figure 5. These are overall molecular dissociation quantum yields for which the contribution due to the different channels could not be isolated. Note the quantum yields are obtained from photodissociation cross sections assuming gas-phase absorption cross sections for H_2S in Ar. The validity of this assumption was verified in Kr.¹³ To provide a further characterization of the system, measurements were carried out on D_2S in Ar. IR spectra showed that the samples were always contaminated with H_2S , and indeed both SH and SD could be observed in the LIF probe during photodissociation. This served as a useful method for obtaining relative dissociation quantum yields of the two isotopes, in the same solid, under identical conditions. A clearly measurable difference between the two isotopes $\phi^{\text{H}}/\phi^{\text{D}} = 1.5 \pm 0.02$ is observed at 193 nm.

IV. Discussion

(A) Initial State. Infrared spectra of H_2S isolated in Ar and Kr matrices were studied as a function of dilution and temperature, concentrating on the ν_1 transition which is the strongest absorption

band in these matrices. A typical spectrum was shown in ref 13. The monomer absorption occurs at 2582.5 and 2575.5 cm^{-1} in Ar and Kr, respectively. Dimer absorption bands can be clearly identified at 2569.6 and 2566 cm^{-1} in Ar and Kr, respectively. These are in agreement with prior assignments.²⁷ The monomer shows a single sharp absorption line even at a spectral resolution of 0.1 cm^{-1} . In contrast with H_2O spectra,²⁸ there are no rotational sidebands. In effect, H_2S is locked in place, with a fixed molecule-lattice geometry while H_2O is established by IR²⁸ and neutron scattering studies²⁹ to be a nearly free rotor in the same matrices. The freezing of motion in the case of H_2S is presumably due to its larger size, i.e., due to repulsive interactions between the lone electron pairs on sulfur and rare gas atoms. If so, the potential energy of a substitutional H_2S molecule can then be expected to be at a minimum when the electron pairs point at the largest cavities in the unit cell, i.e., at six atom O_h sites bisecting the sides of the unit cell. This in turn would force both SH bonds, which are at nearly right angles to each other, to point directly at Kr atoms. Such a prealignment would be expected to bias photodissociation dynamics, as will be discussed below.

(B) Final Products. The presented emission spectra, the radiative lifetimes, and the thermal behavior of sulfur atoms in Kr directly parallel those of atomic oxygen.⁵ In the latter case, using well-determined gas-phase pair potentials, it was possible to construct solid-state potential energy surfaces and to reproduce the observed spectra by Monte Carlo simulations.²¹ In the absence of similar potentials in the case of S-Rg interactions, in the present, we suffice by interpretations in analogy. In an octahedral crystal field, the atomic $^1\text{S} \rightarrow ^1\text{D}$ transition will split into two emission bands $^1A_1 \rightarrow ^1E_g$ and $^1A_1 \rightarrow ^1T_{2g}$. The tighter the trapping site, the larger the separation between the final surfaces. The emission spectra presented in Figure 2a show these features. Both are composed of overlapping bands, with a larger splitting evident in the emission obtained from the higher energy site, site II. Thus, the spectra are consistent with the identification of sites I and II as S atoms trapped in substitutional and interstitial O_h sites, respectively. Observation of both dipole-forbidden bands from each site, with radiative lifetimes significantly shorter than in the gas phase, implies that the transitions are enhanced by cage-induced electric quadrupole.²¹ Accordingly, a greater enhancement and therefore a shorter lifetime are to be expected for the tighter site, in agreement with the observation. Finally, interstitial sites are highly unstable and subject to lower barriers for thermal mobility.²⁴ The conversion from the high-energy site II to the low-energy site I upon partial annealing of the solid is a further consistency check of the assignment of these sites to interstitial and substitutional S.

In short, upon photodissociation of H_2S in solid Kr, both interstitial and substitutional S atoms are produced. Noting that H_2S does not fit in interstitial sites, it is possible to conclude that the interstitial S atoms are the result of their impulsive ejection into the lattice during the photodissociation of H_2S . Further carrying the analogy between O and S atoms, this process is only consistent with the cage exit of S atoms while on the ^1D surface.²⁴ The requirement of kinetic energy to eject an S atom over the cage barrier, along with the observation that this channel is present even at the longest excitation wavelengths, where the total available excess energy is ~ 0.75 eV, would imply that the process proceeds suddenly, prior to energy loss to the lattice. Note, however, that the interstitial production channel is small. Its absolute quantum yield can be estimated from the relative areas in the excitation spectra to be $\sim 1 \times 10^{-3}$. Moreover, the probability of this channel is found to be sensitive to matrix history. These observations indicate that the sudden S atom ejection is controlled at least in part by lattice defects.

The main sulfur atom emission arises from substitutionally trapped species, i.e., in the same trapping site as the parent molecule. Upon annealing of the solids, the excitation spectra of this site undergo a dramatic line narrowing, as illustrated by Figures 2b,c. This is consistent with an atom produced in a

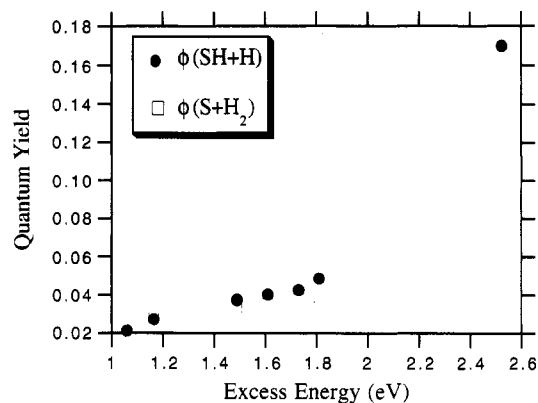


Figure 6. Quantum yield of overall dissociation of H_2S in solid Ar, the sum of S and SH channels. The arrow indicates the expected vertical shift of all data points to account for the S + H_2 channel.

strongly impacted site and therefore consistent with the presence of a nearby H_2 molecule. Note the van der Waals volume of H_2S more than doubles upon formation of S + H_2 . Evidently, the lattice strain is released upon annealing and is likely to be accompanied by separation of the S and H_2 fragments. That sulfur atoms are mobile at the annealing temperature is verified by the observation of formation of S_2 . When annealed at 45 K for a short period of time, a fraction of the original S atoms remain in well-relaxed substitutional sites. This would imply that the H_2 molecule has left the site. While this seems quite unlikely in crystalline solids, it may be induced in matrices by the presence of defects and grain boundaries. These considerations, along with the energetics of the SH + H reaction, would lead us to believe that prior to annealing both $\text{S}(^3\text{P})$ and H_2 must occupy the same dilated substitutional site. It is however notable that no loss of S is observed during its LIF probe in this site, indicating that neither $\text{S}(^1\text{S})$ nor $\text{S}(^1\text{D})$ can react with its neighboring H_2 molecule. $\text{S}(^1\text{S})$ correlates with only highly excited electronic states of H_2S and SH, and as such it is not expected to react with H_2 . It is also well established in the gas phase that $\text{S}(^1\text{S})$ is not quenched by collisions with H_2 .³⁰ At thermal collision energies, $\text{S}(^1\text{D})$ can undergo both insertion and abstraction reactions with H_2 .³¹ Yet, we do not see any evidence of such reactions. Evidently, there is an activation barrier on this surface, which is large enough to prevent reaction at cryogenic temperatures. To our knowledge, there are no surfaces for the $\text{S}(^1\text{D}) + \text{H}_2$ system with sufficient accuracy to establish this fact. In the analogous case of $\text{O}(^1\text{D}) + \text{H}_2$, for which there are many refined surfaces, there is a variance in predictions on the presence of a barrier.³² In very recent studies of O-doped solid D_2 in our laboratory, we have observed the $\text{O}(^2\text{S}) \rightarrow (^1\text{D})$ emission to be stable with irradiation time and concluded that indeed there is a barrier to the $\text{O}(^1\text{D}) + \text{D}_2$ reaction, which is not surmountable at cryogenic temperatures.³³ In the present, we have to conclude that there is a barrier on the $\text{S}(^1\text{D}) + \text{H}_2$ global surface, which is sufficiently large as to prevent reaction at encounter energies of 15 K.

(C) Cage Exit of H. The previously reported absolute photodissociation quantum yields of H_2S in Kr matrices, ϕ , are for total dissociation probabilities, i.e., $\phi = \phi(\text{SH}) + \phi(\text{S})$.¹³ Combining the presently measured branching ratios with the previously obtained absolute photodissociation quantum yield of H_2S , it is possible to derive absolute quantum yields of the individual product channels, viz.

$$\phi(\text{S}) = \phi\gamma(\text{S}) \quad \text{and} \quad \phi(\text{SH}) = \phi(1 - \gamma(\text{S})) \quad (6)$$

The resulting quantum yields for individual channels are plotted as a function of excess energy in Figure 6. Note, not ϕ but $\phi(\text{SH})$ is the cage exit probability of H atoms. Within experimental error, $\phi(\text{S})$ is nearly independent of energy. As a result, $\phi(\text{SH})$, or equivalently the H atom cage exit probability, follows the energy dependence of total photodissociation, ϕ . Thus, the present

measurements do not change the prior conclusions with respect to the nature of H atom ejection in the photodissociation of H₂S.¹³ The main observation is the absence of an abrupt energetic threshold in $\phi(\text{SH})$, which is in contrast with the original observations in the case of matrix-isolated H₂O.^{8b} In the more recent revised analysis, the absorption thresholds of H₂O in Ar and Kr are reassigned to coincide with the observed photodissociation threshold.¹¹ In Xe, it is still believed that the true dissociation threshold is being observed since it occurs above the absorption threshold.¹¹ It should be noted that the red wing of absorption in Xe is matrix induced, with an origin that is subject to some speculation.¹¹ The lowest energy for which we have a measurement, 0.75 eV, is simply determined by the absorption threshold and H₂S.¹³ It is important to note that we verify that the dissociation near threshold does not involve a subset of the molecules, ones that may be trapped near defects. This is established by carrying the process to completion—in all measurements, we verify that the entire H₂S content is depleted by photodissociation. Thus, cage exit is observed for energies significantly below ~ 1.7 eV,⁹ which remains to be believed as the experimentally extracted sudden barrier for H atom ejection from H₂O in Kr.¹¹ Accordingly, our results would seem to be in contradiction with those of H₂O, and a significant contribution from delayed cage exit must be inferred at low excess energies. We return to this issue in greater detail after presenting a theoretical treatment of the sudden process.

(D) Cage-Induced Reactions. Referring to the energy level diagram of Figure 1, we note that, due to the multiplicity of electronic surfaces, several product channels exist that need to be considered. In an earlier study in Kr matrices, the direct photodissociation of H₂S to produce S(¹S) + H₂ has been observed at energies between 7.5 and 8.5 eV.³⁴ In the presently studied energy range, the S(¹S) + H₂ channel opens up in the 193-nm measurement. Yet we do not observe S(¹S \rightarrow ¹D) emission during photodissociation, nor do we observe any abrupt change in yields. For example, an increase in the yield of the S channel over that of the recombination to H₂S could have been expected. In fact, the trend is the opposite; namely, the SH:S branching ratio nearly doubles upon opening of this channel. This is consistent with the notion that at high excess energies the photodissociation becomes dominated by sudden exit of H (see below) and the fact that S(¹S) does not directly correlate with neither ¹A₁ nor ¹B₂ surfaces which are initially accessed.

The S(¹D) channel is open throughout the range of studied energies. Since only the singlet excited states of H₂S are prepared with the laser, spin conservation requires that the direct production of H₂ from H₂S(¹A₂ or ¹B₁) proceed on the H₂(¹ Σ_g) + S(¹D) surface. In the case of the indirect reaction, after rattling of SH(²I) and H(²S) in the cage, triplet products may become accessible after curve crossings. To yield permanent products from the energized ¹D channel, either efficient spin conversion or separation of the products by cage exit of S or H₂ is required. Efficient spin conversion due to avoided crossings between surfaces that arise from S(¹D) and S(³P) in rare gas lattices is to be expected.²¹ A lower limit for this process can be inferred from recent gas-phase studies which show that spin conversion of S(¹D) proceeds by ~ 5 collision with rare gas atoms.³⁵ As discussed above, and in analogy with O atoms, observation of interstitial S is indicative of ejection into the lattice on the ¹D surface.^{21,36} In short, there is evidence for direct production of S(¹D) in the S + H₂ channel. However, in the main H₂ + S channel, which terminates as in cage S(³P) the measurements cannot separate between a reaction that proceeds on the triplet surface versus one that involves S(¹D) production followed by spin conversion to S(³P).

The permanent products of the in-cage SH + H reaction are S(³P) crowded by a nearby H₂ molecule or recombination to yield H₂S. The recombination is favored by a ratio of $\sim 20:1$. This ratio should in principle reflect the accessible phase space volumes associated with each of the product channels in the

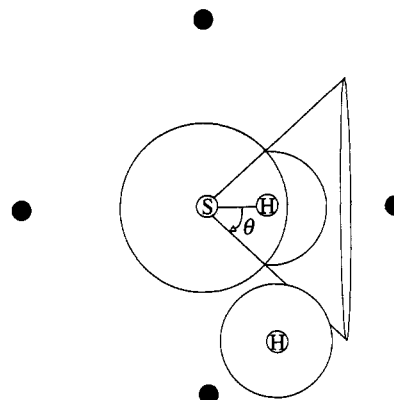


Figure 7. Definition of the reaction cone for in-cage H + SH reaction. Also shown are the nearest-neighbor Kr atoms (dark circles) to indicate the possible biasing of recombination due to blockage by SH-Kr binding.

energized system. To first order, we may expect geometric factors to determine this ratio. Consider the caged fragments with an excess energy of order 1 eV, significantly above the SH + H reaction barrier. The system loses its energy to the lattice by collisions. Whether H₂S or S + H₂ is formed should then be determined by the probability that the energy loss at the barrier separating the two products occurs on the SH...H side or HS...H side, the two configurations being distinguished by their reaction cones. Associating Ω with the solid angle of acceptance for the S + H₂ channel, in the absence of any dynamical biases, $\Omega/4\pi$ is the probability of this channel. The experimental S + H₂ channel probability of the caged system is given as

$$\phi_{\text{recomb}}(\text{S}) = \frac{\phi(\text{S})}{1 - \phi(\text{SH})} \approx 0.042 \quad (7)$$

This probability remains nearly constant throughout the studied energy range. The ratio would imply a reaction cone half-angle of $\theta = 23^\circ$. This may be compared with the geometric angle derived from the space-filling type model illustrated in Figure 7 as $\theta = \arctan(R_{\text{H}}/R_{\text{SH}}) = 30^\circ$, where $R_{\text{H}} = 1.2 \text{ \AA}$ is the van der Waals radius of H while $R_{\text{SH}} = 1.39 \text{ \AA}$ is the sum of covalent radii of S and H. The observation of a value of θ smaller than the geometric value would in principle imply a preference to the H...SH side attack. This bias is consistent with the fact that the SH radical shows a $\sim 2000\text{-cm}^{-1}$ well for hydrogen bonding to Kr.²⁰ In effect, after extensive energy loss, Kr acts as a protecting group for H from attack along the H...HS coordinate. A literal interpretation of the geometric factor in itself maybe somewhat naive: an observed cone angle of 23° is close to the geometric value of 30° . Another indication of steric control of the in-cage reaction is the near independence of the branching ratio on initial excess energy. Thus, within the framework of this analysis, it can be concluded that on the time scale of recombination the relative orientations of the reagents are well randomized and that nearly the full range of relative orientations between SH and H is accessible. Clearly, the in-cage reaction must be regarded as that of SH + H as opposed to a direct reaction on the H₂S excited surface.

V. Statistical Treatment of Sudden Cage Exit

(A) The Model. By the sudden limit of cage exit we understand separation of fragments over a barrier which is potential in nature—an adiabatic cage barrier which cannot respond to the dynamics of the fragment. This limit should be particularly appropriate for the present case of a light fragment exiting over barriers that are determined by the spatial configuration of heavy atoms. Included in the sudden limit is the possibility of cage exit after multiple unsuccessful tries, as long as the energy loss of the fragments does not significantly distort the cage. The term delayed exit is used to describe deviation from the sudden limit.

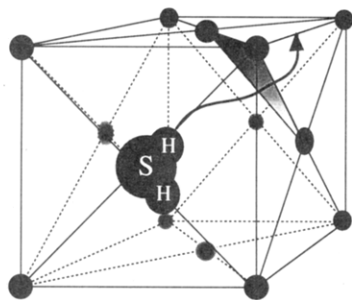


Figure 8. The rare gas unit cell is shown with a substitutionally trapped H₂S molecule. The arrow indicates a possible reaction coordinate to produce permanent dissociation by trapping the H atom at the nearest octahedral interstitial site. The minimum-energy path to this location takes the H atom through the triangular window which is indicated by the shaded area.

TABLE 1: Model Parameters

	Ar	Kr	Xe
lattice constant (Å) ^a			
5 K	5.280	5.646	6.130
15 K	5.284	5.650	6.133
30 K	5.330	5.664	6.145
$V(L-J)_{Rg-Rg}$ ^b			
σ (Å)	3.4	3.65	3.98
ϵ (cm ⁻¹)	84	113.17	161
$V(B-M)_{H-Rg}$ ^c			
β (Å ⁻¹)	3.34	3.31	3.068
A (eV)	787.4	1186.7	1023.3
symmetric stretch frequency, ω (cm ⁻¹):			
5 K	46.4	36.0	32.8
15 K	46.0	35.8	32.65
30 K	42.3	34.9	32.0
equilibrium position, q_0 (Å) ^d			
5 K	2.173	2.325	2.527
15 K	2.174	2.327	2.529
30 K	2.188	2.33	2.532
$\xi\sqrt{2}$ (Å) ^d			
5 K	0.113	0.089	0.0723
15 K	0.114	0.092	0.0789
30 K	0.134	0.111	0.093

^a From ref 40. ^b From ref 38. ^c From ref 41. ^d Parameters of barrier height distribution in eq 15 of text.

Although the term is somewhat unfortunate, since it invokes timing of the fragment as opposed to the cage, we retain it for historical reasons. The opposite extreme to sudden exit is exit over a fully relaxed barrier which is of free energy nature, such as a potential of mean force. This is the limit appropriate for the description of thermally activated barrier hops which govern diffusion of point defects. Where it prevails, simulations are invaluable to the description of the nonequilibrium dynamics of delayed exit, which according to our definition spans the full spectrum of behaviors between the two extreme limits. Statistical treatments, which provide nontrivial insights, are possible in the limiting cases. Below, we present a formulation of the sudden cage exit limit and compare the predicted absolute quantum yields to our experimental data to characterize the observed dynamics.

A schematic of the parent molecule trapped in a substitutional site is given in Figure 8. Permanent dissociation requires that the H fragment reach a stable product site, namely, the interstitial octahedral site. The minimum-energy path connecting the reagent to products corresponds to passage of the H atom through one of the triangular faces that joins the octahedron to the substitutional site. The barrier then corresponds to the minimum energy of the planar HRg₃ complex. Assuming no lattice distortions, the Rg₃ configurations are dictated by the thermal distribution of three mutual nearest neighbors in the pure lattice, $\langle P(r_1, r_2, r_3) \rangle$. This distribution arises from both zero-point and thermal fluctuations. A distribution of Rg₃ configurations in turn implies a distribution of potential barriers, $P(V_b)$, which plays the major role in the statistics of cage exit probabilities. We may associate

with a given Rg₃ configuration a window cross section, $\sigma(E, V_b)$, which depends on the fragment excess energy, E , and is defined by the area of the triangle for which $E > V_b$. A collision with this window can lead to exit, while a collision with the rest of the triangle—the cage wall—leads to energy loss. The fragment can then have multiple attempts at exit, until its energy drops below the threshold of the V_b distribution. Several scenarios, aimed at elucidating possible structural or dynamical biases, can then be considered for the multiple attempts at cage exit which define the experimentally observable quantum yield. The model should be able to explain energy, temperature, pressure, isotope, and host dependences of cage exit quantum yields.

(a) *Barrier Height Distribution.* The distribution of three mutual nearest neighbors in the lattice can be obtained by a variety of methods, by simulations, or by normal-mode analysis. In all cases, for the cryogenic temperatures of interest, it is crucial to include zero-point contributions to lattice fluctuations. To provide a nearly analytical theory, we use the vibrational normal modes of the Rg₃ system, and we note that since the position distributions are dominated by zero-point motion, it is sufficient to consider the symmetric stretch of Rg₃ in the average field of all other atoms. The distribution in positions can then be equated with the probability density of positions of a quantum harmonic oscillator at thermal equilibrium³⁷

$$\langle P(r_1, r_2, r_3) \rangle_{r_n, n>3} = \rho(Q, T) \quad (8)$$

where

$$\rho(Q, T) = \frac{1}{\xi\sqrt{\pi}} \exp\left(-\frac{Q-Q_0^2}{\xi^2}\right) \quad \text{and} \quad \xi = \sqrt{\frac{\hbar}{\mu\omega} \coth\left(\frac{\hbar\omega}{k_B T}\right)} \quad (9)$$

in which Q is the symmetric stretching coordinate of Rg₃. The vibrational frequency, ω , can then be extracted from the second derivative of the potential along Q

$$\omega = \sqrt{\frac{k}{\mu}}, \quad k = \frac{\partial^2 \langle V(Q) \rangle_{r_i}}{\partial Q^2} \quad (10)$$

in which the averaging implies a summation over all lattice points held at their equilibrium positions. The potential along Q is evaluated using Lennard-Jones (L-J) parameters for Rg–Rg interactions, under the assumption of pairwise additivity

$$\langle V(Q) \rangle = \langle V(q_1, q_2, q_3) \rangle_{r_{i>3}} = \frac{1}{2} \sum_{i=1}^3 \sum_{j=1}^n V(\bar{r}_i - \bar{r}_j) \quad (11)$$

and

$$V(\bar{r}_i - \bar{r}_j) = V(r) = 4\epsilon \left[\left(\frac{\sigma}{r}\right)^{12} - \left(\frac{\sigma}{r}\right)^6 \right] \quad (12)$$

Based on the correspondence principle, when using reduced parameters, $E^* = E/\epsilon$ and $r^* = r/\sigma$, all rare gases yield the same L-J potential, and accordingly, once the oscillator force constant is evaluated, the distribution function in eq 9 can be evaluated for all Rg.³⁸ In practice, significant error is made by this approach since the L-J parameters are a poor representation of the true many-body interactions.³⁹ Without resorting to more refined potentials, we use the experimental temperature-dependent lattice constants of the various solids⁴⁰ and then use the L-J parameters for the evaluation of $V(Q)$. The minimum configuration, Q_0 , and to a minor extent the frequency, ω , will accordingly show a temperature dependence. The parameters used and the derived frequencies for Ar, Kr, and Xe are collected in Table 1.

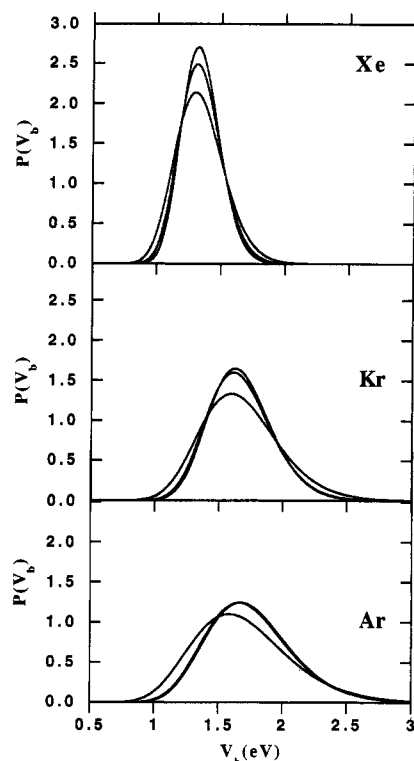


Figure 9. Normalized barrier height distributions in Xe, Kr, and Ar, at three different temperatures each: 5, 15, and 30 K.

The interaction of an H atom with its neighbors, in the plane of the triangle, is highly repulsive, and the interaction range is limited to the amplitude of the symmetric breathing mode, δQ . As such, V_{H-Rg} is well represented by the Born–Mayer (B–M) form

$$V_{H-Rg} = Ae^{-\beta r} \quad (13)$$

The potential parameters A and β , obtained from ref 41, are collected in Table 1. For a given configuration of Rg_3 , the potential barrier V_b is defined as the minimum energy and therefore occurs for the H atom placement at the center of the symmetric triangle. With a coordinate origin placed at the center of mass, defining $q_i = r_{cm} - r_i$ and noting that for the symmetric stretch $|q_1| = |q_2| = |q_3| = q$, we obtain

$$V_b = 3Ae^{-\beta q} \quad (14)$$

The single particle distribution, $\rho(q, T)$, is obtained from $\rho(Q, T)$ by identifying μ in eq 9 as the rare gas atomic mass and noting that $\langle V(q, T) \rangle = \langle V(Q, T) \rangle / 3$. Given the single particle distribution for the symmetric stretch motion, and the fact that V_b is a single valued function of q , the distribution of V_b can be obtained analytically:

$$P(V_b, T) dV_b = \rho(q, T) dq \quad (15a)$$

$$P(V_b, T) = \rho(q, T) \frac{dV_b}{dq} = \frac{\rho(q, T)}{dV_b/dq} \quad (15b)$$

$$= \frac{1}{\sqrt{\pi\xi\beta V}} \exp\left[-\left(\frac{1}{\beta} \ln(V/3A) + q_0\right)^2 / \xi^2\right] \quad (15c)$$

This distribution plays the central role in determining cage exit probabilities in the present treatment.

The barrier height distributions of eq 15c are shown in Figure 9 for three different temperatures—5, 15, and 30 K—for Ar, Kr, and Xe. They correspond to Gaussians skewed by the gradient of the H–Rg potential (eq 15b). The distributions make it clear

that the notion of a cage exit barrier, without reference to its distribution, can be quite misleading. Even at 0 K, which in the case of Ar is identical to the 5 K distribution shown in Figure 9, due to the zero-point fluctuations of the lattice, a wide distribution in V_b arises. As an example, the full width at half-maximum of the 0 K distribution in Ar is ~ 0.8 eV. The higher is the barrier, the broader is its distribution due to the denominator in eq 15b. Due to the lighter mass, and accordingly the larger frequency of the symmetric stretch (see Table 1), in Ar, and to a lesser extent in Kr, the distributions up to 15 K are dominated by the zero-point energy. Broadening of the distributions due to thermal contributions becomes evident in Ar and Kr at 30 K, while in Xe the effect is noticeable starting from 5 K (Xe is nearly classical at 5 K). At 30 K, the distribution in the case of Ar shows a significant shift to lower energies. This is the result of the thermal expansion of the lattice (see Table 1), which at this temperature is only significant in the case of Ar.

(b) *Exit Probabilities.* To cross the barrier, the projectile need reach the window of the triangle wall, the area for which $E > V_b$. Thus, a transmission probability $\kappa(E, V_b)$ can be defined as the ratio of window-to-wall area

$$\kappa(E, V_b) = \sigma(E, V_b)_{\text{window}} / \sigma(V_b)_{\text{wall}} \quad (16)$$

where $\sigma(V_b)_{\text{wall}}$ is simply the area of the symmetric triangle identical by its potential barrier, and $\sigma(E, V_b)_{\text{window}}$ is the area enclosed within the equipotential $E = V_b$. Near threshold conditions, for $(E - V_b)/V_b \leq 1$, κ can be well approximated as (see Appendix)

$$\begin{aligned} \kappa(E, V_b) &= g \left(\frac{4(E - V_b)}{\beta^2 V_b} \right) / \frac{3\sqrt{3}}{4} q^2 \\ &= 5.8 \frac{(E - V_b)}{V_b \ln^2(V_b/3A)} \end{aligned} \quad (17)$$

Here g is a shape factor for the window, which is a symmetric triangle with rounded vertices. Its value is obtained by fitting to numerically computed values of κ . Note, here we are satisfied with the threshold behavior. At high excess energies, where the quantum yields may reach saturation, this approximation is not sufficient.

The single trial cage exit probability can now be defined by taking the full barrier distribution into account:

$$\begin{aligned} \phi(E) &= \int_{V_b=0}^{V_b=E} \kappa(E, V_b) P(V_b) dV_b \\ &= \int_{V_b=0}^{V_b=E} \frac{5.8}{\ln^2(V_b/3A)} \left[\frac{E}{V_b} P(V_b) - P(V_b) \right] dV_b \end{aligned} \quad (18)$$

This is also the quantum yield of sudden cage exit for systems in which the fragment and host atom masses are comparable, such that after a failed trial the collisional energy loss lowers the kinetic energy of the fragment below the threshold value of V_b . The single trial exit probabilities, ϕ_1 , for Ar and Kr are shown in Figures 10 and 11, respectively. In the case of large mass asymmetry, as in the present, after a failed trial the fragment may remain above V_b and therefore will have successive chances at cage exit. To determine the multiple trial exit probabilities, it is useful to express $\phi(E)$ in a simple analytical form. A power law in terms of $E - E_{th}$ is sufficient for this purpose:

$$\phi(E) = a(E - E_{th})^n \quad (19)$$

The parameters a and n for Ar, Kr, and Xe at 15 K are collected in Table 2. Note that this fit and the definition of E_{th} are somewhat arbitrary. It is obtained from a linear plot of $\phi(E)$ vs E . Near E_{th} , the cage exit probability takes a precipitous drop due to the

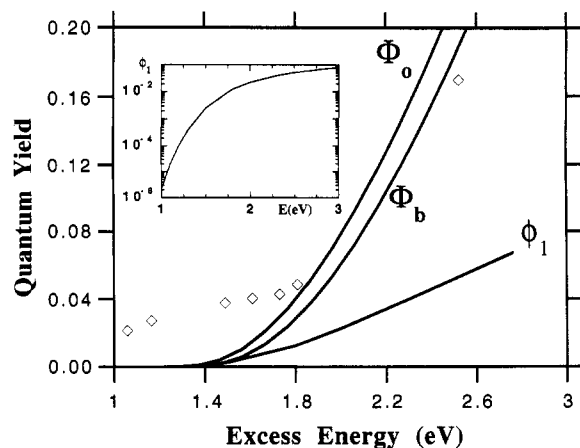


Figure 10. Quantum yields of H exit in Kr at 15 K. The single trial probability, ϕ_1 , the multiple trial probability with window orientation, Φ_0 , and wall orientation, Φ_b , are shown together with the experimental data for H exit (open diamonds). In the inset, a semilogarithmic plot of ϕ_1 is shown to illustrate the precipitous drop of probabilities near threshold.

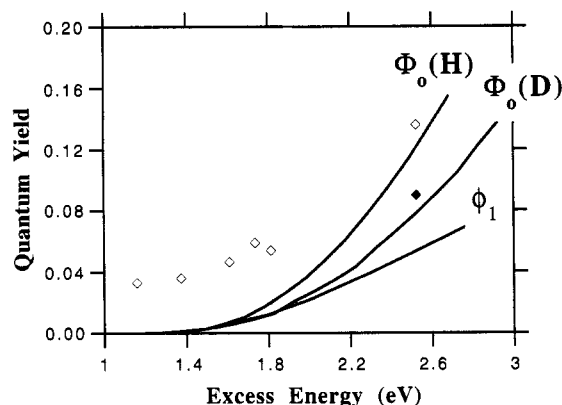


Figure 11. Quantum yields of H and D exit in Ar. The curves are theoretical predictions for single trial of H, ϕ_1 (H), for multiple trial with window orientation of H and D, Φ_0 (H) and Φ_0 (D). The open diamonds are the experimental data for total dissociation probability of H_2S , and the filled diamond is the total dissociation probability of D_2S .

nearly Gaussian tail of the barrier height distribution and the logarithmic drop in the transmission probability, κ . This is shown in the case of Ar in the inset to Figure 10.

The *multiple trial exit probabilities* can be obtained subject to initial orientational biases. To do this, we note that at the relevant excess energies, where $E \gg k_B T$, the binary collision assumption is valid, whereupon a head-on collision the fractional energy loss by the fragment, $\Delta E/E$, is given as $4mM/(m+M)^2$. Defining

$$\gamma = 1 - \Delta E/E \quad (20)$$

the energy of the fragment after suffering n collisions is

$$E_n = \gamma^n E \quad (21)$$

It may be argued that the collisional energy loss should be averaged over impact parameters, in which case the energy loss per collision is $\gamma/2$. However, in the case of grazing collisions with the wall, multiple scattering occurs. As such, energy loss of γ between trials is a more realistic assumption, which is also verified by the molecular dynamics simulations.¹ Thus, to compute the multiple trial probabilities of cage exit, we assume that between each trial the fragment will undergo a full collisional energy loss. Accordingly, after n trials (where $n = \text{Int}[\ln(V_{th}/V)/\ln(\gamma)]$) the fragment falls below the threshold V_b and the sudden exit channel is shut off. To take recrossing probabilities into account, we assume that the fragment after crossing the barrier to the stable octahedral trapping site may, after a collision and loss of energy,

TABLE 2: Power Law Parameters for Quantum Yields of Cage Exit^a

	Ar	Kr	Xe
single trial probability, $\phi(E)^b$			
a	0.034	0.0387	0.055
E_{th} (eV)	1.25	1.3	1.1
n	1.79	1.44	1.275
$\Phi_0(H)^c$			
a	0.083	0.18	0.396
E_{th} (eV)	1.31	1.39	1.17
n	2.02	1.66	1.86
$\Phi_b(H)^d$			
a	0.06	0.168	0.36
E_{th} (eV)	1.4	1.45	1.1
n	2.15	1.675	2.41
$\Phi_0(D)^e$			
a	0.05	0.195	0.22
E_{th} (eV)	1.3	1.44	1.16
n	2.02	1.52	1.9
$\Phi_b(D)^f$			
a	0.05	0.082	0.19
E_{th} (eV)	1.3	1.47	1.19
n	2.02	1.78	2.1

^a The parameters are for the different cage exit probabilities fitted to the power law form of eq 19 in the text. ^b Single trial exit probability, eq 18 of text. ^c Quantum yield for H exit with initial window orientation, eq 22 of text. ^d Quantum yield for H exit with initial wall orientation, eq 23 of text. ^e Same as footnote c, but for D exit. ^f Same as footnote d, but for D exit.

recross the same barrier with 1/8 probability (eight triangular walls to an octahedron). Accordingly, the probabilities per trial can be listed and summed to obtain the overall quantum yield, Φ . For an initial parent-lattice orientation such that the R-H bond points at a window, the quantum yield is given as

$$\text{first try: } \phi_1(E) = \phi(E) - \frac{1}{8}\phi(\gamma E) \quad (22a)$$

$$\text{second try: } \phi_2(E) = (1 - \phi_1(E))\phi(\gamma E) - \frac{1}{8}\phi(\gamma^2 E) \quad (22b)$$

$$\text{nth try: } \phi_n(E) = (1 - \sum_{i=1}^{n-1} \phi_i(E))\phi(\gamma^n E) - \frac{1}{8}\phi(\gamma^n E) \quad (22c)$$

$$\text{quantum yield: } \Phi_0 = \sum_{j=1}^n (\phi_j(E)) \quad (22d)$$

For a nonrotating molecule with the R-H bond locked along the Rg atoms, the first collision is doomed to failure at cage exit. The fragment loses energy, and the first trial with exit possibility occurs at an energy γE . Accordingly, and including recrossing probabilities as above, the quantum yield of cage exit for this initially blocked geometry, Φ_b , can be computed as

$$\text{first try: } \phi_1(E) = \phi(\gamma E) - \frac{1}{8}\phi(\gamma^2 E) \quad (23a)$$

$$\text{second try: } \phi_2(E) = (1 - \phi_1(E))\phi(\gamma^2 E) - \frac{1}{8}\phi(\gamma^3 E) \quad (23b)$$

$$\text{nth try: } \phi_n(E) = (1 - \sum_{i=1}^{n-1} \phi_i(E))\phi(\gamma^n E) - \frac{1}{8}\phi(\gamma^{n+1} E) \quad (23c)$$

$$\text{quantum yield: } \Phi_b = \sum_{j=1}^n (\phi_j(E)) \quad (23d)$$

Computing the same quantities for the case of isotopic substitution, as in H vs D exit, simply requires redefinition of γ in eq 20.

Near the threshold for cage exit, $\Phi < 0.2$, it is convenient to represent the energy dependence of quantum yields in the form of the power law of eq 19. The parameters of such fits, for the different initial orientation biases, for H and D exit, and in different rare gas crystals at 15 K, are tabulated in Table 2. $\Phi_0(\text{H})$ and $\Phi_0(\text{D})$ are shown in Figure 10 for 15 K Kr. The deviation between these curves in the case of Xe is negligible, while in the case of Ar it is larger than that of Kr: as the number of attempts increases, the effect of initial bias becomes less important on the overall exit probability. In the case of free rotors, the quantum yield will be bracketed by these two limits. In the case of hydrides, even if the parent molecule does not rotate freely, the effect of orientational bias should be small due to the large amplitude of librational motion. Note, however, that the orientational bias can be dramatic in the case where the number of trials is small, either near threshold energies or for cases where the mass of the projectile is comparable to that of the host atoms. The extreme case occurs where the exit is determined by the single trial probability, in which case if initially oriented toward the window ϕ of eq 18 applies while if oriented toward the wall the exit probability becomes zero. In the latter case, the exit probability should be controlled by the rotational dynamics of the parent molecule. Such prealignment effects have already been observed for heavy atoms. In the case of F_2 , the cage exit probability is larger at 4.5 K than at 12 K,⁴² which has been interpreted as due to freezing of the molecule into a cone directly pointing at the exit window, in agreement with simulations.⁴³ In molecular dynamics simulations, the cage exit probability of Cl atoms upon photodissociation of Cl_2 at low excess energies is observed to be determined by the onset to rotation.⁴⁴ In this case, based on the potentials used, at low temperatures the molecule is frozen pointing at the walls. More recently, in the case of photodissociation of ozone in solid Ar, the quantum yields of dissociation have been found to be determined by an activation energy consistent with the rotational barrier.⁴⁵ Using the proper guest–host potentials in the presented formulation, it should be possible to treat photofragments other than H by including the initial angular distribution of the parent-lattice orientations.

The isotope effect in cage exit probabilities is nontrivial. At a given excess energy, the probabilities of H versus D exit depend on the number of trials prior to falling below E_{th} . In Figure 11 we show the isotope effect on Φ_0 in Ar. A significant isotope effect is observed. However, in terms of the power law analysis, it can be seen in Table 2 that the main isotope effect on Φ_0 is in the preexponent: neither E_{th} nor n could be experimentally distinguishable. In the case of Φ_0 in Ar, there is no discernible isotope dependence as can be verified by the entries in Table 2. This is not the case in Kr, where the number of trials is much larger, and therefore an isotope effect is discernible in both exponents and E_{th} for either orientational bias.

We point out that the power law fit to the quantum yields in the threshold region is merely a convenience, which allows direct comparisons with experiment and simulation. The limits of validity of the presented model extend beyond the threshold limit. To illustrate this, we show the predicted saturation behavior in Xe in Figure 12. This is obtained by using a polynomial fit to ϕ_1 and the approximation to κ given in eq 17. In the case of Xe, it can be seen in Figure 12 that the quantum yield saturates at $\Phi_0 \sim 0.75$, at an excess energy of ~ 3.5 eV.

(C) Comparison with Experiment. Prior to making comparisons in absolute cage exit probabilities, the errors involved in the experiment should be put in perspective. The major source of errors in the experiment arise from the determination of absorption coefficients in the solid. Measurement of absorption coefficients in the UV in the solid suffers from errors introduced due to uncertainty in number density of the dopant and due to scattering. Systematic errors in this determination can arise from the presence of clusters and impurities, which should be carefully eliminated. The second source of error is due to estimation of the irradiation photon fluence, which requires a careful characterization of laser

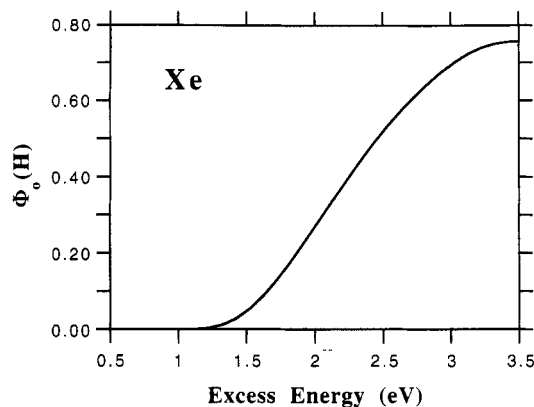


Figure 12. Saturation of photodissociation quantum yields in Xe, based on the sudden exit dynamics.

spot size in the overlap volume between photodissociation laser and probe laser. In our measurements, laser spot sizes are measured by scanning a pinhole mounted on a micrometer stage and by making corrections for geometric factors associated with beam overlap and incidence angle. Thus, absolute quantum yields are subject to errors of order 30%. Relative quantum yield measurements are subject to much smaller errors and can usually be reproduced with 5%. In general, trends in quantum yields as a function of energy, temperature, etc., are well determined; however, one needs to be careful in assessing the significance of absolute probabilities.

The model developed above predicts absolute probabilities of cage exit; the same quantity was derived experimentally in the case of H_2S in Kr. The comparison is shown in Figure 10. The limited data above 1.8 eV are in agreement with the model prediction, and the sudden model for cage exit is an acceptable description at these energies. What is also clear is that the data at energies below 1.3 eV cannot be rationalized by sudden exit by any stretch of the model. At 1 eV, where a finite cage exit probability of 0.02 is observed, the predicted quantum yield is $\sim 10^{-6}$.

In the case of measurements in Ar, only the overall dissociation probability of H_2S is available. If we make the reasonable assumption that the $\text{S} + \text{H}_2$ channel has a quantum yield similar to that of Kr, then a nearly vertical downshift of these points by 0.02 should represent $\phi(\text{H})$. With this consideration in mind, the Ar data show the same trend as in the case of Kr: the sudden exit limit is reached at excess energies > 1.8 eV. At lower energies exit over thermalized barriers must be inferred. Another interesting test of the sudden limit is through the isotope effect. At 193 nm, the quantum yield of $\phi(\text{H}_2\text{S}) = 1.5\phi(\text{D}_2\text{S})$. This is in exact agreement with the sudden exit model of eq 22, when γ is replaced by its value of D–Ar collisions. Note, however, that at this excess energy eq 23 shows almost no isotope dependence. We therefore conclude that the SH bonds in $\text{H}_2\text{S}/\text{Ar}$ point at the windows.

In conclusion, in the case of H_2S , both sudden and delayed exit contribute to photodissociation. This sudden dynamics dominates at high excess energies, however, cage exit of H also occurs at energies significantly below the threshold of potential barriers. This description is in good agreement with the latest molecular dynamics simulations on HCl/Xe .¹² The delayed exit dynamics is also supported by the observation of nearly statistical in-cage chemistry, as obtained from the branching ratio between recombination and bimolecular reaction. The latter implies that the energetic fragments upon recoil have ample time to sample the phase space of the bimolecular encounter, during which thermalization occurs, and therefore opening of the cage windows is to be expected—a model, in good agreement with the earlier simulations of HI dissociation in Xe.¹ More quantitative comparisons with simulations are not possible at present, due to the limited statistics in the existing simulations. It should also be emphasized that we find the barrier height distribution, and

therefore the zero-point motion of the lattice atoms, to play a major role in determining the quantum yields of dissociation. As such, one should be careful in making comparisons with classical simulations, especially in the case of predicted temperature dependences. An approximate method of making allowance for zero-point energies is to scale the temperature of classical simulations.⁴⁶

As to the photodissociation of H₂O in rare gas matrices, it is instructive to compare the experimental data with the present statistical model. Firstly, it should be noted that the main seeming contradiction between the H₂O data and that of H₂S, and the early molecular dynamics simulations, was the observation of a sharp threshold in the photodissociation quantum yields. This discrepancy, in the case of Ar and Kr, no longer exists. Reanalysis of the absorption spectra now establishes that the observed threshold is the onset of absorption, and therefore little can be said about the presence of a photodissociation threshold.¹¹ It is nevertheless believed that in the case of Xe the photodissociation threshold is being observed; however, the absorption onset there is at best matrix induced and requires further characterization with respect to its role in photodissociation.⁴⁷ The experimental data pertain to excess energies above ~1.7 eV in the case of Ar and Kr and above ~1.3 eV in the case of Xe. At these excess energies the photodissociation should be dominated by sudden exit. The data in H₂O are then possible to compare to the present, especially since they have been given in terms of the power law of eq 19. For this comparison we use the parameters reported prior to the most recent reanalysis and take into account that the reported E_{th} values are artificial. The reported exponents of the power law in Ar, Kr, and Xe at 5 K are 2.1, 1.76, and 2.5.⁹ Inspection of Table 2 shows that these are well within experimental error of the statistical model predictions as long as the blocked geometry in Xe is assumed. For Φ_b , the exponents are 2.15, 1.7, and 2.41 in Ar, Kr, and Xe, respectively. A strong isotope dependence of preexponents $H/D = 1.66$ is observed in Ar. As in the case of H₂S, this is only consistent with the behavior of Φ_0 where, from Ar $H/D = 1.66$ is predicted (see Table 2). The comparison of preexponents should be done with care since it entails absolute quantum yields, which are subject to large experimental error. In a consistent set of data, the ratio of preexponents for H exit may be a more meaningful comparison. Data have been reported from such a set.⁹ The observed ratio of preexponents, Ar:Kr:Xe, is 1:1.4:3.7 in the experiment. Thus, if we choose from Table 2 Φ_0 for Ar and Φ_b values for Kr and Xe, the theoretical prediction for the ratio of preexponents Ar:Kr:Xe is 0.8:1.7:3.6. It is possible to also compare absolute quantum yields. In Ar at an excess energy of 2.6 eV (160 nm), the absolute quantum yield of dissociation is reported as 20%,^{8b} the predicted value for Φ_0 is 16% (see Figure 11). Although H₂O is a nearly free rotor, it would seem from the present comparison that in Ar the O–H bond orientation is biased toward the windows, while in Kr and Xe it is biased toward the walls. Under this assumption a nearly perfect agreement arises for all comparable observables: isotope effect in Ar; ratio of preexponents in Ar, Kr, Xe; and exponents in all three rare gases. Finally, experimentally, a significant temperature dependence in the range 5–30 K is observed only in Ar.¹⁰ The temperature dependence of sudden exit arises from the barrier height distribution. As already pointed out, and depicted in Figure 9, due to the thermal expansion of the lattice, in this temperature range the barrier height distribution shifts to lower energies in Ar. Accordingly, we expect a significant temperature dependence in Ar, and a more minor one in the heavier rare gases (see Figure 9). Thus, temperature dependence of sudden exit can be explained consistently, without invoking local heating, which arises from delayed dynamics.¹⁰

We conclude that indeed in the case of H₂O, sudden exit dynamics is being observed, which seems completely consistent with the predictions of the statistical theory presented here. The results are also consistent with H₂S data for high excess energies of 1.7 eV and above, where the sudden dynamics becomes the

dominant mode of cage exit. The reason the delayed exit contributions have not been observed in H₂O seems to be simply due to Franck–Condon factors which do not allow observation of dissociation near, or below the threshold of sudden exit, where delayed dynamics dominates.

VI. Conclusions

Time-independent measurements of reactive dynamics in solids can be characterized by determination of structure and sites of parent and photofragments via spectroscopy, measurements of probabilities of individual reactive channels as a function of energy, mass asymmetry, and thermodynamic variables such as temperature and pressure. Statistical treatments of dynamics are invaluable to the extraction of the information content in such measurements. In this paper we have presented experimental measurements on the photodissociation of H₂S isolated in Ar and Kr matrices, and a statistical theory for absolute rates of sudden cage exit probabilities was delineated.

Infrared spectra of H₂S isolated in Ar and Kr matrices give no evidence of rotation of the molecule. Upon excitation to the first absorption continuum, H₂S dissociates via several distinct channels which were identified based on the spectroscopy of products. The site specific spectroscopy of atomic sulfur, which we presented and analyzed in analogy with atomic oxygen,²¹ has been particularly useful for this purpose. The reactive channels that could be identified are (a) permanent dissociation in H + SH, with cage exit of H; (b) permanent dissociation into S + H₂ with cage exit of S atoms, as evidenced by the generation of interstitial S; and (c) in-cage reaction between H and SH photofragments to yield either S + H₂ in a strongly distorted cage or recombination as H₂S. Absolute probabilities of each of these channels were determined in Kr. The cage-induced bimolecular reaction could be interpreted as statistical, controlled by the cone of reaction of SH + H. A small deviation from the purely statistical behavior is rationalized as partial blockage of the reaction cone by Kr, due to the hydrogen bonding between SH and Kr.²⁰ It was also noted that S(¹D) does not react with H₂ upon a 15 K encounter, implying that there is a barrier to this reaction. At high excess energies, the cage exit of H is dominated by sudden dynamics, i.e., by adiabatic exit over potential barriers of the cage. At low excess energies, it is dominated by delayed exit, after energy transfer and distortion of the cage. This conclusion is made by reference to the statistical model predictions in Ar and Kr and the isotope dependence in Ar. Agreement with the latter test is only successful if the parent S–H bond points at a cage window. Domination by sudden dynamics at high excess energy, and delayed at low excess energy, is in accord with the results of the latest molecular dynamics simulation on HCl/Xe.¹²

The presented statistical treatment is based on the realization that even at 0 K a large distribution in cage exit barriers arises due to the zero-point amplitude of fluctuations in positions of the host lattice. Typically, the fwhm of the barrier height distribution is half as wide as its most probable value. This distribution, which could be expressed analytically, plays the key role in determining quantum yields of sudden cage exit. By defining an energy-dependent transmission coefficient, absolute cage exit probabilities could be computed for multiple trials and different orientational biases. The resulting quantum yields are in good agreement with the high-energy data in H₂S and seem to be in quantitative agreement with all reported measurements (isotope, temperature, host, and energy dependences) of H₂O dissociation in rare gas matrices. Quite clearly the observed photodissociation in the case of H₂O is dominated by sudden dynamics. However, this is mainly a result of the energy regime of the measurements. Evidently,¹¹ in the case of H₂O, Franck–Condon factors do not allow access of the threshold region where delayed dynamics would be expected to dominate the molecular dissociation. At present, there are no obvious contradictions among the experi-

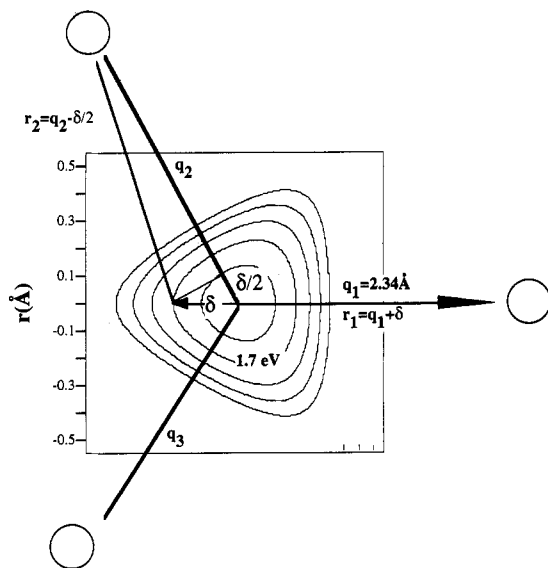


Figure 13. The equipotentials are shown, with a spacing of 0.1 eV, for three Kr atoms at $q = 2.34$ Å, which corresponds to $V_b = 1.54$ eV. The window at $E = 1.7$ eV occurs at $\delta/q \sim 0.1$. The locations of the Kr atoms are not to scale.

mental studies or the molecular dynamics simulations. The major source of confusion in the past seems to have stemmed from uncertainties concerning the absorption spectrum of H₂O in the solid state and the modification of potentials in its first absorption continuum.^{11,47}

It would be useful to test the detailed predictions of the presented theory vis-a-vis both experiment and simulation. We note that since there are no well-prescribed methods for the incorporation of zero-point effects in molecular dynamics simulations, comparisons with simulations should be done with care. It is also worth noting that it is in the description of delayed exit dynamics that simulations will play the major role in establishing a more detailed understanding of the nonequilibrium processes that control the many-body dynamics of fragment-cage-lattice interactions and energy flow.

Finally, we note that extension of the presented statistical formulation to photofragments other than H should be straightforward. In fact, the formulation should be more generally applicable for heavier photofragments, since as the mass asymmetry between fragment and host is reduced, photodissociation should increasingly become dominated by sudden exit. In this limit, as discussed in the text, orientational biases may play the major role in determining quantum yields of permanent dissociation. Such molecular-lattice prealignment effects have already been observed in the case of F₂,^{42,24} Cl₂,⁴⁴ and most recently O₃.⁴⁵

Acknowledgment. Support by the US Air Force Phillips Laboratory under Contract S04611-90-K-0035 and support from AFOSR under a University Research Initiative F49620-1-0251 is gratefully acknowledged. The participation of D. G. Imre in the early stages of the experiments on H₂S and thoughts of N. Blake and N. Schwentner on the early stages of the development of the statistical model are acknowledged.

Appendix. The Transmission Coefficient near Threshold

The energy-dependent transmission coefficient, κ , was defined in eq 16 of the text as the ratio of window to wall areas. The wall area, $\sigma(V_b)_{\text{wall}}$, is simply defined as the area of the symmetric triangle constructed by the three mutual nearest-neighbor rare gas atoms, where $V_b = 3A \exp(-\beta q)$ is the potential experienced by an H atom at the center of the triangle. The area of the window, $\sigma(E, V_b)$, is defined by the area contained in the equipotential at E for a given triangle geometry characterized by V_b . Referring to Figure 13, for an H atom placed at a small

extension from the center such that $r_1 = q_1 + \delta$, and as long as $\delta/q \ll 1$, the separations from the other vertices can be approximated as $r_2 = r_3 \sim q - \delta/2$. Associating the energy E with such an eccentric atom, consider the fractional excess energy

$$\frac{E - V_b}{V_b} = \frac{A[e^{-\beta(q+\delta)} + 2e^{-\beta(q-\delta/2)} - 3e^{-\beta q}]}{3Ae^{-\beta q}} \quad (\text{A1.1})$$

$$= \frac{1}{3}[e^{-\beta\delta} + 2e^{+\beta\delta/2} - 3] \quad (\text{A1.2})$$

$$\approx \frac{1}{4}\beta^2\delta^2 \quad (\text{A1.3})$$

in which the final approximation is reached by expanding the exponentials in (A1.2) in series and retaining terms up to second order. The window area is proportional to δ^2 with a proportionality constant that can be identified as the geometric shape factor, g . Referring to Figure 13, the geometric average of the areas of a symmetric triangle of height $3\delta/2$ and a circle of radius δ should be a good approximation for the window geometry, since it is bounded by these two shapes. Although this yields an acceptable approximation, we rely on numerical integration to obtain a more reliable value. The quantity of interest is κ

$$\begin{aligned} \kappa(E, V_b) &= \frac{\sigma(E, V_b)_{\text{window}}}{\sigma(V_b)_{\text{wall}}} \\ &= g \left(\frac{4(E - V_b)}{\beta^2 V_b} \right) / \frac{3\sqrt{3}}{4} q^2 \\ &= g \left(\frac{4(E - V_b)}{\beta^2 V_b} \right) / \frac{3\sqrt{3}}{4} \left(\frac{\ln(V_b/3A)}{\beta} \right)^2 \quad (\text{A2}) \\ &= g' \frac{(E - V_b)}{V_b \ln^2(V_b/3A)} \end{aligned}$$

κ was calculated by numerical integration of the area enclosed by equipotentials $E = V_b$ to $E = 3.5$ eV with increments of 0.1 eV, for triangles characterized by V_b values ranging from 1 to 2.5 eV. $g' = 5.8$ was then obtained from the slope of a linear fit to the plot of $\kappa V_b \ln^2(V_b/3A)$ vs $E - V_b$ for the full set of data. The fit is good to within a few percent for $(E - V_b)/V_b \sim 1$, i.e., quite satisfactory near the threshold region. The average deviation is $\sim 10\%$ for $(E - V_b)/V_b \sim 2$ values. However, polynomial fits or the exact numerical values of κ are necessary near the saturation limit, where higher order terms to the expansion of (A1.2) contribute.

References and Notes

- (1) Alimi, R.; Gerber, R. B.; Apkarian, V. A. *J. Chem. Phys.* **1988**, *89*, 1974.
- (2) Alimi, R.; Gerber, R. B. *Chem. Phys. Lett.* **1990**, *173*, 393.
- (3) Kunttu, H.; Seetula, J.; Rasanen, M.; Apkarian, V. A. *J. Chem. Phys.* **1992**, *96*, 5630.
- (4) Lawrence, W. G.; Apkarian, V. A. *J. Chem. Phys.*, in press.
- (5) Lawrence, W. G.; Okada, F.; Apkarian, V. A. *Chem. Phys. Lett.* **1988**, *150*, 339.
- (6) Lawrence, W. G. Thesis, University of California at Irvine, 1991.
- (7) Schriever, R.; Chergui, M.; Unal, O.; Stepanenko, V.; Schwentner, N. *J. Chem. Phys.* **1989**, *91*, 4128.
- (8) (a) Schriever, R.; Chergui, M.; Unal, O.; Schwentner, N.; Stepanenko, V. *J. Chem. Phys.* **1990**, *93*, 3245. (b) Schriever, R.; Chergui, M.; Schwentner, N. *J. Chem. Phys.* **1990**, *93*, 9206.
- (9) Schriever, R.; Chergui, M.; Schwentner, N. *J. Phys. Chem.* **1991**, *95*, 6124.
- (10) Tarasova, E. I.; Ratner, A. M.; Stepanenko, V. M.; Fugol, I. Ya.; Chergui, M.; Schriever, R.; Schwentner, N. *J. Chem. Phys.* **1993**, *98*, 7786.
- (11) Chergui, M.; Schwentner, N.; Stepanenko, V., submitted.
- (12) Gersonde, I. H.; Gabriel, H. *J. Chem. Phys.* **1993**, *98*, 2098.

- (13) Zoval, J.; Imre, D.; Ashjian, P.; Apkarian, V. A. *Chem. Phys. Lett.* **1992**, *19*, 549.
- (14) Chergui, M.; Schwentner, N. *Trends Chem. Phys.* **1992**, *2*, 89.
- (15) Lawrence, W. G.; Apkarian, V. A. *J. Chem. Phys.* **1992**, *97*, 2229.
- (16) Gole, J. L. *J. Phys. Chem.* **1980**, *84*, 1333.
- (17) Ball, d. W.; Kafafi, Z. H.; Hauge, R. H.; Margrave, J. L. *A Bibliography of Matrix Isolation Spectroscopy*; Rice University Press: Houston, 1988.
- (18) Heumann, B.; Weide, K.; Duren, R.; Schinke, R. *J. Chem. Phys.* **1993**, *98*, 5508. Flouquet, F. *Chem. Phys.* **1986**, *13*, 257.
- (19) Ben-Nun, M.; Levine, R. D. *J. Phys. Chem.* **1992**, *96*, 1523.
- (20) Zoval, J.; Imre, D.; Apkarian, V. A. *J. Chem. Phys.* **1993**, *98*, 1.
- (21) Danilychev, A. V.; Apkarian, V. A. *J. Chem. Phys.* **1994**, *100*, 5556.
- (22) Murray, J. R.; Rhodes, C. K. *J. Appl. Phys.* **1976**, *47*, 5041.
- (23) Taylor, R. V.; Walker, W. C. *Appl. Phys. Lett.* **1979**, *35*, 359.
- (24) Danilychev, A. V.; Apkarian, V. A. *J. Chem. Phys.* **1993**, *99*, 8617.
- (25) Hirst, D. M.; Guest, M. F. *Mol. Phys.* **1982**, *46*, 427.
- (26) Hsu, C.-W.; Liao, C.-L.; Ma, Z.-X.; Tjossemann, P. J. H.; Ng, C. Y. *Chem. Phys. Lett.* **1992**, *199*, 78.
- (27) Barnes, A. J.; Howells, J. D. R. *J. Chem. Soc., Faraday Trans.* **1972**, *268*, 729.
- (28) Redington, R. L.; Milligan, D. E. *J. Chem. Phys.* **1962**, *37*, 2162.
- (29) Langel, W.; Schuller, W.; Knozinger, E.; Flegler, H. W.; Lauter, H. *J. Chem. Phys.* **1988**, *89*, 1741. Knozinger, K.; Schuller, W.; Langel, W. *Faraday Discuss. Chem. Soc.* **1988**, *86*, 1.
- (30) Black, G.; Sharpless, R. L.; Slanger, T. G.; Lorents, D. C. *J. Chem. Phys.* **1975**, *63*, 4551. Dunn, O. J.; Filseth, S. V.; Young, R. A. *J. Chem. Phys.* **1973**, *59*, 2392.
- (31) Gunning, H. E.; Stauss, O. P. *Adv. Photochem.* **1966**, *4*, 143.
- (32) Whitlok, P. A.; Muckerman, J. T.; Fisher, E. R. *J. Chem. Phys.* **1982**, *76*, 4468 and references therein.
- (33) Danilychev, A. V.; Apkarian, V. A. Manuscript in preparation.
- (34) Scott, W.; Walker, W. C. *Appl. Phys. Lett.* **1982**, *41*, 1047.
- (35) Nan, G.; Houston, P. L. *J. Chem. Phys.* **1992**, *97*, 7865.
- (36) Lawrence, W. G.; Apkarian, V. A. *J. Chem. Phys.* **1992**, *97*, 6199.
- (37) Cohen-Tannoudji, C.; Diu, B.; Laloe, F. *Quantum Mechanics*; Wiley Interscience: Paris, 1977; Vol. I.
- (38) Kittel, C. K. *Introduction to Solid State Physics*, 5th ed.; J. Wiley: New York, 1976.
- (39) Inert Gases: Klein, M. L., Ed.; Springer Series in Chemical Physics; Springer: New York, 1984; Vol. 34, Chapter 1.
- (40) Rabinovich, V. A.; Vasserman, A. A.; Nedostrup, V. I.; Veksler, L. S. *Therophysical Properties of Neon, Argon, Krypton, and Xenon*; National Standard Reference Service of the USSR, A series of Property Tables; Hemisphere: New York, 1988.
- (41) Tang, K. T.; Toennies, J. P. *Chem. Phys.* **1991**, *156*, 413.
- (42) Kunttu, H.; Apkarian, V. A. *Chem. Phys.* **1990**, *171*, 423.
- (43) Alimi, R.; Gerber, R. B.; Apkarian, V. A. *J. Chem. Phys.* **1990**, *92*, 3551.
- (44) Alimi, R.; Brockman, A.; Gerber, R. B. *J. Chem. Phys.* **1989**, *91*, 1611.
- (45) Benderskii, A. V.; Wight, C. A. *J. Chem. Phys.*, submitted.
- (46) Bergsma, J. P.; Berens, P. H.; Wilson, K. R.; Fredkin, D. F.; Heller, E. H. *J. Phys. Chem.* **1984**, *88*, 612.
- (47) Chergui, M.; Schwentner, N. *Chem. Phys. Lett.* **1994**, *219*, 237.